Supporting Information for "Pre-industrial, present and future atmospheric soluble iron deposition and the role of aerosol acidity and oxalate under CMIP6 emissions"

Elisa Bergas-Massó[1,2], María Gonçalves Ageitos[1,2], Stelios Myriokefalitakis[3], Ron L. Miller[4], Twan van Noije[5], Philippe Le Sager[5], Gilbert Montané Pinto[1], Carlos Pérez García-Pando[1,6]

[1]Barcelona Supercomputing Center (BSC), Barcelona, Spain

[2]Universitat Politècnica de Catalunya (UPC), Barcelona, Spain

[3]Institute for Environmental Research and Sustainable Development (IERSD), National Observatory of Athens, Penteli, Greece

[4]NASA Goddard Institute for Space Studies, New York, NY, US

[5]Royal Netherlands Meteorological Institute (KNMI), De Bilt, the Netherlands

[6]ICREA, Catalan Institution for Research and Advances Studies, Barcelona, Spain

Contents of this file

Figure S5: Fe solubilization budgets by source and atmospheric processing mechanism for the perturbed-dust scenarios

Table S1: Fe deposition rates by time-period in the literature

Table S2: Fe emission rates by source and time-period in the literature

Text S1:

1. Data Analysis

1.1. Relative Differences between Scenarios

When comparing fields from different scenarios, the PD simulation is always taken as reference. Differences in fields of extensive variables are shown as relative differences in % as in Equation 1.

$$RD(X)_{scenario_i} = \frac{X_{scenario_i} - X_{PD}}{X_{PD}} \cdot 100 \tag{1}$$

where $RD(X)_{scenario_i}$ refers to the relative difference of variable X for the $scenario_i$. $X_{scenario_i}$ and X_{PD} is the mean value among ensemble members of the variable X for the $scenario_i$ and the PD scenario respectively.

1.2. Statistical Test

When representing relative changes between scenarios with its spatial distribution, a statistical test is carried on to only show relative changes that are statistically significant. Here we use the t-test to compare the 30 ensemble values in each grid cell between simulations. The level of statistical significance is expressed as a p-value between 0 and 1. Following this procedure, we mask all grid-cells where p-values are lower than 0.05 (Student, 1908).

1.3. Ensemble spread

To have a measure of the ensemble spread (e.g., the difference between the 30 members of the same ensemble) we compute the standard deviation (σ) with respect to the ensemble mean (X) as shown in Equation 2.

$$\sigma = \sqrt{\frac{1}{N}\sum_{i=1}^{N}(x_i - X)^2} \tag{2}$$

where N is the number of ensemble members, x_i is the value of a variable x in a grid cell for the member i, and X is the ensemble mean for that variable x in that grid cell.

1.4. Acidity in terms of the pH

The acidity level of a solution can be quantified based on the thermodynamic activity of dissolved hydrogen ions (H^+). This measure of acidity is reported as a dimensionless quantity known as the pH. Here we use pH as a diagnostic of acidity computed based on the H^+ molality (m_{H^+}):

$$pH = -\log_{10}(m_{H^+}) \tag{3}$$

pH values reported in this study are computed by averaging monthly pH values, where data points with no water is not considered and pH values lower than 0 are masked and set to 7 and values between 0 and 1 are set to 1 . Those transformations are done to correct the pH overestimation caused in areas with low relative humidity by the metastable assumption in the thermodynamic equilibrium model.

Figures S1 to S5

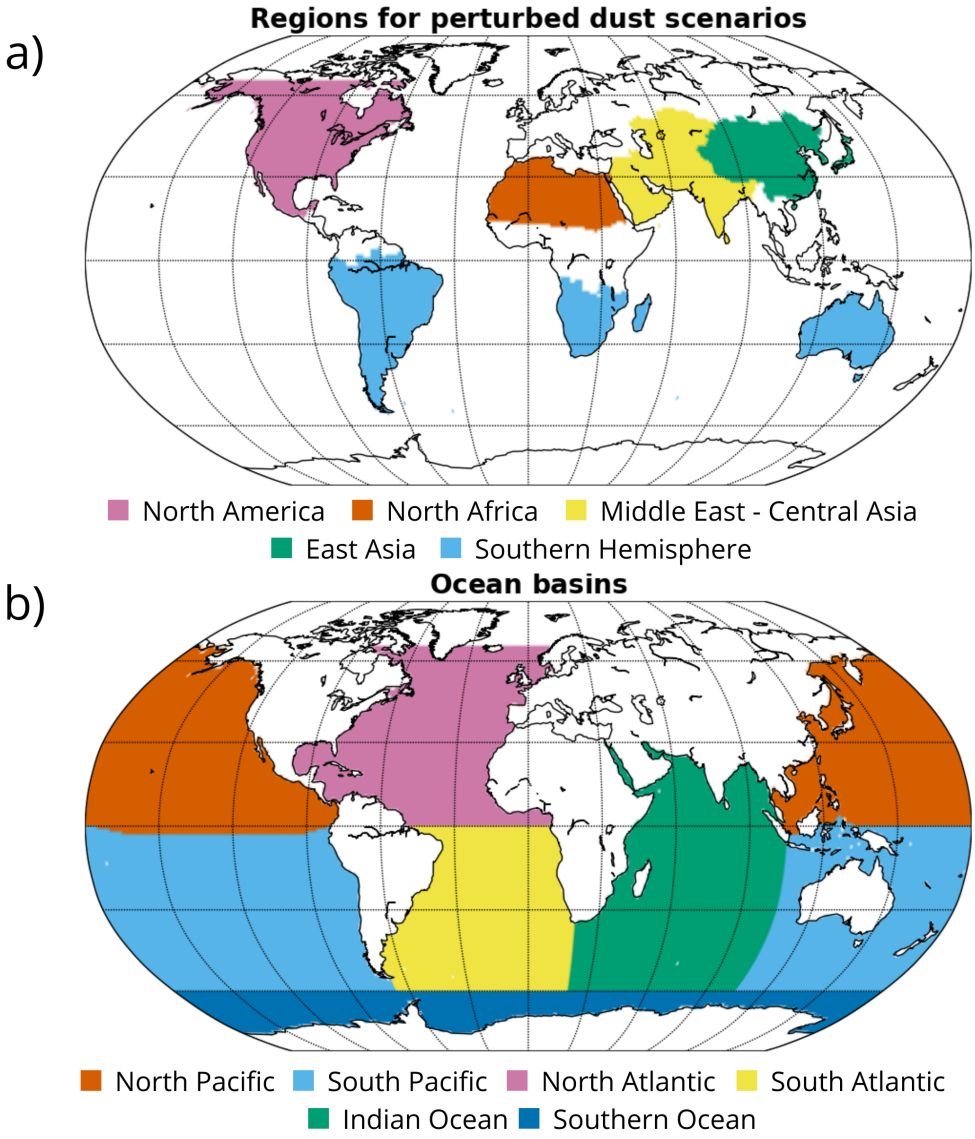

Figure S1. Regions defined for (a) perturbed dust scenarios and (b) analysis of deposition in different ocean basins. Regions are based on the defined ones by the HTAP project (Koffi et al., 2016)

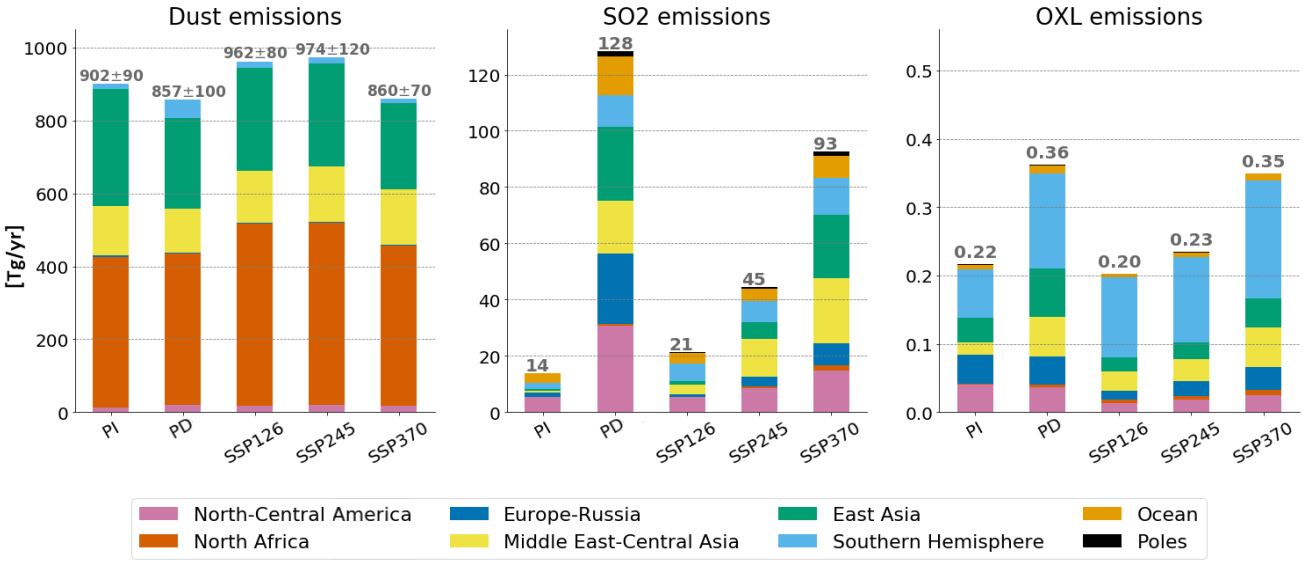

Figure S2. Mean annual emissions in Tg/yr of dust (right figure), sulfur dioxide (SO_2) (middle figure) and oxalate (OXL) (right figure) for each of the scenarios considered. The different colors represent the contribution of the different HTAP regions considered to the total emission budget.

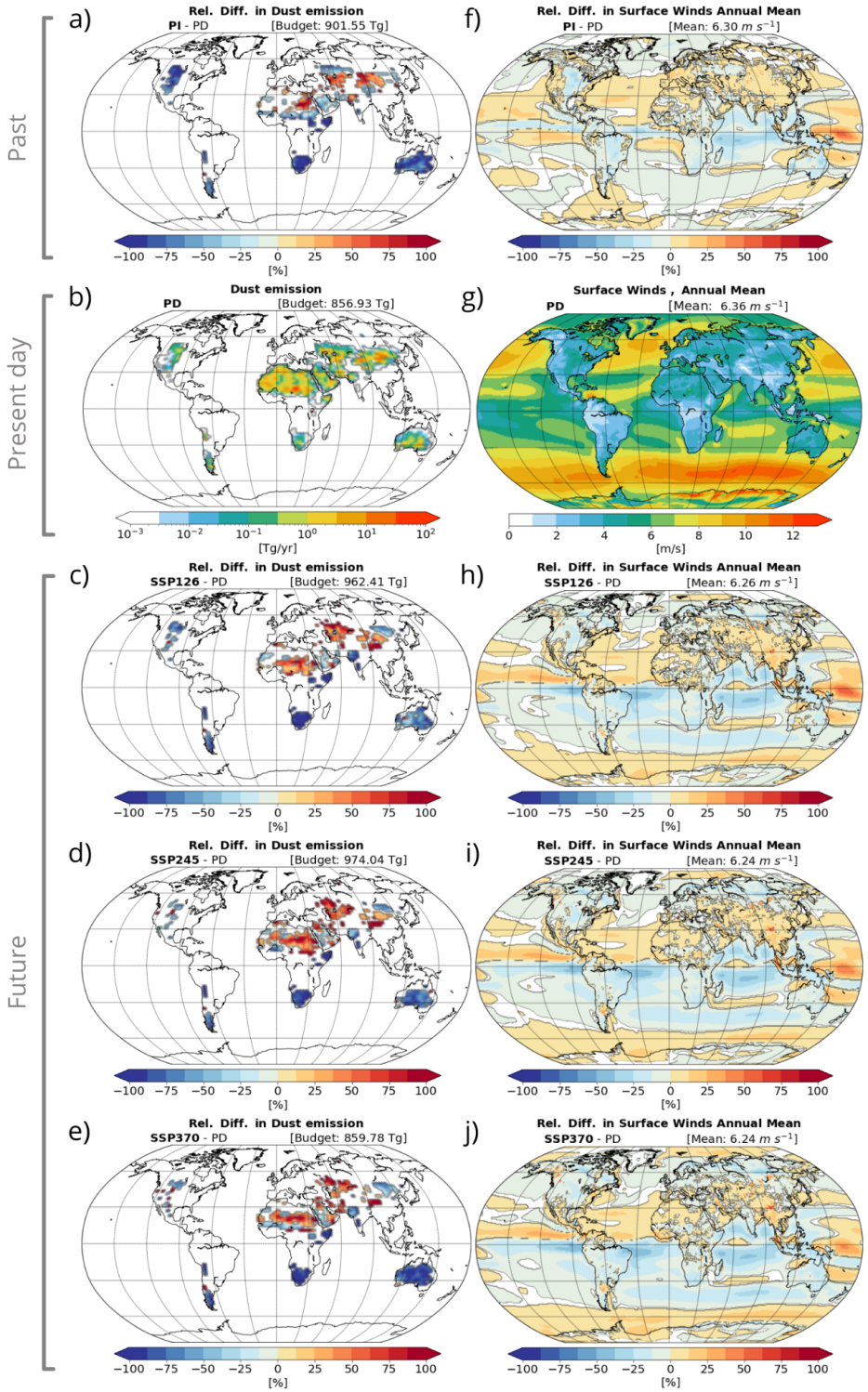

Figure S3. Mean annual dust emission (Tg/yr) for the PD scenario (b) and relative differences (%) in the estimates for the PI (a) and the future scenarios SSP1-2.6 (c), SSP2-4.5 (d), and SSP3-7.0 (e) with respect to the PD, mean annual surface winds (m s^{-1}) for the PD scenario (g) and relative differences (%) in the estimates for the PI (f) and the future scenarios SSP1-2.6 (h), SSP2-4.5 (i), and SSP3-7.0 (j) with respect to the PD (f,h,i,j).

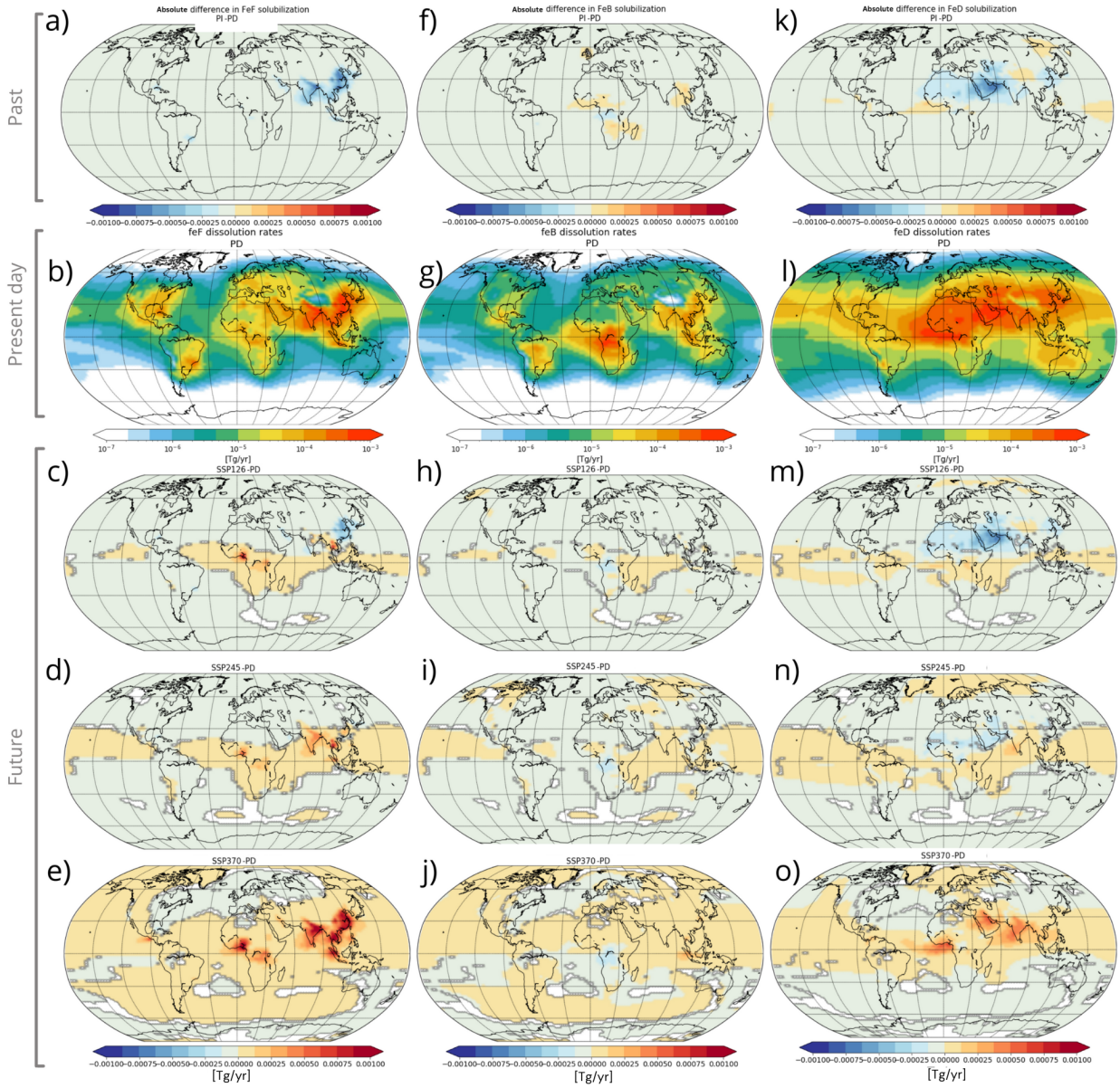

Figure S4. Mean annual dissolution rate for PD for FeF (b), FeB (g) and FeD (l) for the PD. Absolute differences of the mean annual dissolution rate for FeF, FeB and FeD in the PI (a,f,k), and the future scenarios SSP1-2.6 (c,h,m), SSP2-4.5 (d,i,n) and SSP3-7.0 (e,j,o) with respect to the PD.

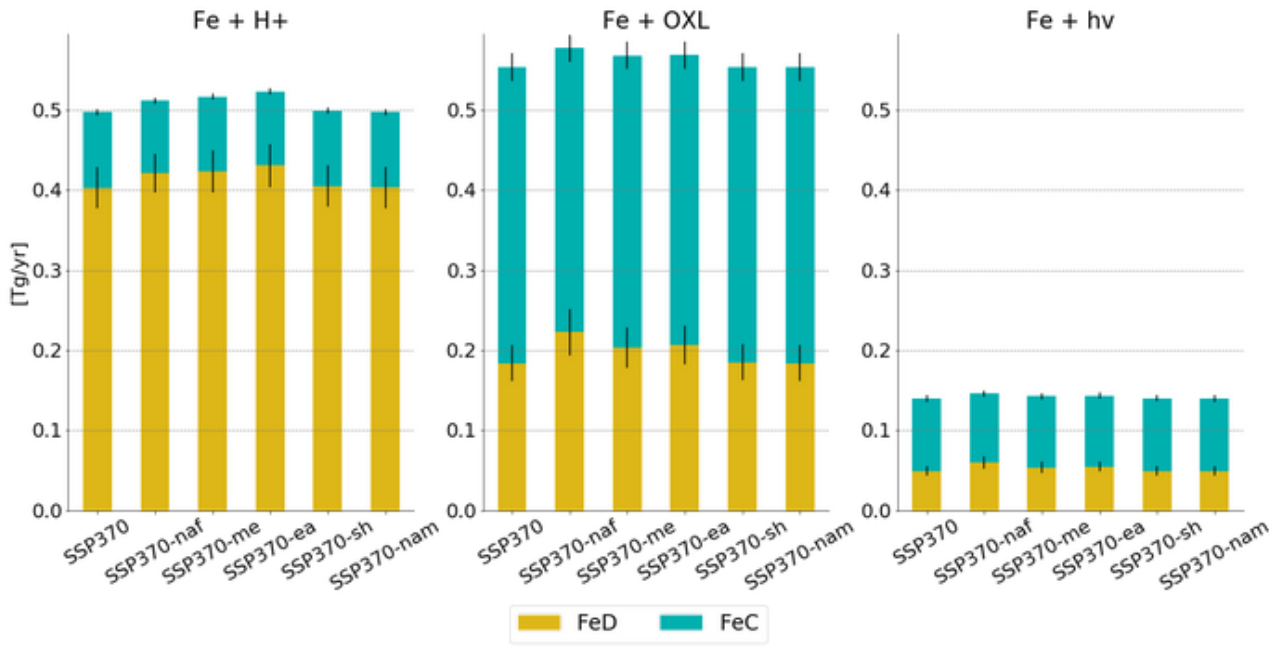

Figure S5. Fe solubilization budgets for the different perturbed-dust scenarios and atmospheric processing mechanisms: acidic dissolution (left), oxl-promoted dissolution (middle), and photoreductive dissolution budgets (right). Solubilization of Fe from dust sources (FeD) is represented with the yellow-orange colour and solubilization of Fe from combustion sources (FeC) (i.e., both from biomass burning, FeB, and anthropogenic sources, FeF) is represented in blue-green colour. Black bars indicate the budget spread for the 30 ensemble members.

Tables S1 to S2

Table S1. Annual deposition rates of total Fe and soluble Fe (Tg Fe/yr) over the open ocean for pre-industrial (PI), present day (PD) and future (FU) time in this study and in the literature.

	TFe	SFe		
	PD	PI	PD	FU
This study	12.1 (± 1.4)	0.21 (± 0.01)	0.41 (± 0.01)	0.27-0.56
Myriokefalitakis et al. (2020)		0.18-0.23	0.28-0.35	0.24-0.30
Hamilton et al. (2020)		0.46-0.70	0.70-0.76	0.77
Hamilton et al. (2019)	12-26		0.50-0.53	
Ito et al. (2019)	16 (± 7)		0.26 (± 0.12)	
Myriokefalitakis et al. (2018)	17 (± 7)		0.30 (± 0.09)	
Scanza et al. (2018)	18.5		0.59	
Ito and Shi (2016)	10.2	0.051-0.067	0.11-0.12	
Myriokefalitakis et al. (2015)	6.964	0.063	0.19	0.136
Johnson and Meskhidze (2013)			0.26	
Luo and Gao (2010)			0.34	
Luo et al. (2008)		0.1	0.21	

Table S2. Annual emission rates of total Fe (Tg Fe/yr) from dust, anthropogenic and fire sources for pre-industrial (PI), present day (PD) and future (FU) time in this study and in the literature.

	Dust iron			Anthropogenic iron			Fire iron		
	PI	PD	FU	PI	PD	FU	PI	PD	FU
This study	42 (± 4)	40 (± 5)	40-46	0.08	1.75	0.97-3.11	0.46	0.52	0.33-0.47
Rathod et al. (2020)					2.2				
Hamilton et al. (2020)	36	57	57	$0.7{\cdot}10^{-3}$ - 0.13	0.68 - 3.4	2.4	1.5 - 2.7	0.94	2.3
Hamilton et al. (2019)		57-130			0.66 - 3.3			1.2 - 2.2	
Scanza et al. (2018)		56.9 - 62.0			2.1 (± 0.51) *				
Myriokefalitakis et al. (2018)		71.5 (± 42.69)			2.1 (± 0.51) *				
Ito and Shi (2016) (2016)	69	69		0.28	0.712		0.66	0.66	
Myriokefalitakis et al. (2015)	35.048	35.048	35.048	0.147	0.768	0.158	0.120	1.200	1.456
Wang et al. (2015)		38.5 - 41			1.2 - 7.2			0.16 - 1.27	
Luo et al. (2008)		54.76						1.07	

November 14, 2022, 6:48pm

References

Hamilton, D. S., Moore, J. K., Arneth, A., Bond, T. C., Carslaw, K. S., Hantson, S., ... Mahowald, N. M. (2020, mar). Impact of Changes to the Atmospheric Soluble Iron Deposition Flux on Ocean Biogeochemical Cycles in the Anthropocene. *Global Biogeochemical Cycles*, *34*(3). doi: 10.1029/2019GB006448

Hamilton, D. S., Scanza, R. A., Feng, Y., Guinness, J., Kok, J. F., Li, L., ... Mahowald, N. M. (2019, sep). Improved methodologies for Earth system modelling of atmospheric soluble iron and observation comparisons using the Mechanism of Intermediate complexity for Modelling Iron (MIMI v1.0). *Geoscientific Model Development*, *12*(9), 3835–3862. doi: 10.5194/gmd-12-3835-2019

Ito, A., Myriokefalitakis, S., Kanakidou, M., Mahowald, N. M., Scanza, R. A., Hamilton, D. S., ... Duce, R. A. (2019). Pyrogenic iron: The missing link to high iron solubility in aerosols. *Science Advances*, *5*(5), 1–11. doi: 10.1126/sciadv.aau7671

Ito, A., & Shi, Z. (2016, jan). Delivery of anthropogenic bioavailable iron from mineral dust and combustion aerosols to the ocean. *Atmospheric Chemistry and Physics*, *16*(1), 85–99. doi: 10.5194/acp-16-85-2016

Johnson, M. S., & Meskhidze, N. (2013). Atmospheric dissolved iron deposition to the global oceans: effects of oxalate-promoted Fe dissolution, photochemical redox cycling, and dust mineralogy. *Geoscientific Model Development*, *6*(4), 1137–1155. doi: 10.5194/gmd-6-1137-2013

Koffi, B., Dentener, F., Janssens-Maenhout, G., Guizzardi, D., Crippa, M., Diehl, T., & Galmarini, S. (2016). *Hemispheric Transport Air Pollution (HTAP): Specification of the HTAP2 experiments*. doi: 10.2788/725244

Luo, C., & Gao, Y. (2010). Aeolian iron mobilisation by dust-acid interactions and their implications for soluble iron deposition to the ocean: A test involving potential anthropogenic organic acidic species. *Environmental Chemistry*, *7*(2), 153–161. doi: 10.1071/EN09116

Luo, C., Mahowald, N., Bond, T., Chuang, P. Y., Artaxo, P., Siefert, R., ... Schauer, J. (2008, mar). Combustion iron distribution and deposition. *Global Biogeochemical Cycles*, *22*(1). doi: 10.1029/2007GB002964

Myriokefalitakis, S., Daskalakis, N., Mihalopoulos, N., Baker, A. R., Nenes, A., & Kanakidou, M. (2015, jul). Changes in dissolved iron deposition to the oceans driven by human activity: a 3-D global modelling study. *Biogeosciences*, *12*(13), 3973–3992. doi: 10.5194/bg-12-3973

-2015

Myriokefalitakis, S., Gröger, M., Hieronymus, J., & Döscher, R. (2020). An explicit estimate of the atmospheric nutrient impact on global oceanic productivity. *Ocean Science*, *16*(5), 1183–1205. doi: 10.5194/os-16-1183-2020

Myriokefalitakis, S., Ito, A., Kanakidou, M., Nenes, A., Krol, M. C., Mahowald, N. M., ... Duce, R. A. (2018, nov). *Reviews and syntheses: The GESAMP atmospheric iron deposition model intercomparison study* (Vol. 15) (No. 21). Copernicus GmbH. doi: 10.5194/bg-15-6659-2018

Rathod, S. D., Hamilton, D. S., Mahowald, N. M., Klimont, Z., Corbett, J. J., & Bond, T. C. (2020, aug). A mineralogy-based anthropogenic combustion-iron emission inventory. *Journal of Geophysical Research: Atmospheres*, e2019JD032114. doi: 10.1029/2019jd032114

Scanza, R. A., Hamilton, D. S., Perez Garcia-Pando, C., Buck, C., Baker, A., & Mahowald, N. M. (2018, oct). Atmospheric processing of iron in mineral and combustion aerosols: Development of an intermediate-complexity mechanism suitable for Earth system models. *Atmospheric Chemistry and Physics*, *18*(19), 14175–14196. doi: 10.5194/acp-18-14175-2018

Student. (1908). The probable error of a mean. *Biometrika*, 1–25. doi: 10.2307/2331554

Wang, R., Balkanski, Y., Boucher, O., Bopp, L., Chappell, A., Ciais, P., ... Tao, S. (2015, jun).

Sources, transport and deposition of iron in the global atmosphere. *Atmospheric Chemistry and Physics*, *15*(11), 6247–6270. doi: 10.5194/acp-15-6247-2015